PERGAMON

Computers & Geosciences 25 (1999) 263–275

COMPUTERS & GEOSCIENCES

A fractional-step finite-element method for the Navier–Stokes equations applied to magma-chamber withdrawal

Arnau Folch [a,*], Mariano Vázquez [b], Ramon Codina [b], Joan Martí [a]

[a] *Institute of Earth Sciences 'Jaume Almera', CSIC, Lluís Solé Sabarís s/n, 08028 Barcelona, Spain*
[b] *International Center for Numerical Methods in Engineering, Universitat Politècnica de Catalunya, Gran Capità s/n, 08034 Barcelona, Spain*

Received 1 December 1997; received in revised form 29 October 1998

Abstract

We develop an algorithm to solve numerically the Navier–Stokes equations using a finite element method. The algorithm uses a fractional step approach that allows the use of equal interpolation spaces for the pressure and velocity fields and can be used to solve both compressible and incompressible flows. The standard Galerkin method is used to space-discretize the equations in which convective terms are dominant because the equations are reformulated in a characteristics co-moving frame providing thus the required artificial diffusion in a consistent way. The algorithm depends on four different parameters. Depending on their values, a fully implicit, a semi-implicit or a fully explicit solution can be obtained. The proposed algorithm may be useful in solving a wide spectrum of problems in geology, engineering and geosciences. Several flows frequently encountered in practical applications such as incompressible, slightly compressible or perfect gas are taken into account. As an example, we use it to model the withdrawal of magma from shallow chambers during explosive volcanic eruptions. Our model constitutes a first attempt to characterize the temporal evolution of the most relevant physical parameters during such a process.

Code available at http.//www.iamg.org/cGEditor/index.htm

Keywords: Navier–Stokes equations; Finite element method; Fractional step method; Explosive volcanic eruptions; Magma chamber withdrawal

1. Introduction

Magmas are silicate melts containing dissolved volatile species whose solubility depends mainly on pressure. At a given temperature and volatile content, there is a critical pressure P_c at which the exsolution of a gas species begins due to oversaturation of the melt. Below this critical pressure, corresponding to a critical depth or exsolution level, the magma behaves approximately as incompressible. In contrast, above the exsolution level, where the pressure is lower than P_c, the magma becomes a compressible two-phase mixture of liquid and dispersed gas bubbles (Sparks, 1978; Papale, 1996). Silicic magma is frequently stored in shallow chambers located a few kilometers below the Earth's surface (Smith, 1979). When pressure inside the chamber is greater than lithostatic, the chamber is said to be overpressured. When the overpressure exceeds the tensile strength of surrounding rocks, a volcanic eruption may be triggered through the propagation of

* Corresponding author. Tel.: +34-3-409-5410; fax: +34-3-411-0012; e-mail: afolch@ija.csic.es

0098-3004/99/$ - see front matter
PII: S0098-3004(98)00164-2

fractures to the surface. The increase in magma pressure necessary to trigger an eruption can be produced either by the addition of new magma into the chamber (Blake, 1981) or by the exsolution of volatiles associated with cooling and crystallization of the magma (Blake, 1984; Tait et al., 1989). In the second situation, the exsolution level must be located inside the chamber.

So far, available numerical simulations of the withdrawal process consider the chamber as an open system; that is, the withdrawal process is driven only by pressure forces associated with magma replenishment and always assume the magma to be incompressible (Spera, 1984; Spera et al., 1986; Trial et al., 1992). Folch et al. (1998) make a first attempt to characterize the temporal evolution of the physical properties of the magma inside the chamber during a volcanic eruption from a closed system, where the eruption is triggered by volatile oversaturation. In such a situation, magma should be treated as an incompressible Newtonian flow below the exsolution level and as a compressible, homogeneous two-phase flow above it. Therefore, an algorithm able to deal simultaneously and well with compressible and incompressible flows is required.

In this paper, the numerical method employed in Folch et al. (1998) is described in detail and extended to other situations of interest in geosciences. We present an algorithm that, using a finite-element method (FEM), numerically solves the Navier–Stokes equations. It uses a fractional-step method which allows the use of equal interpolation spaces for the pressure and the velocity fields and produces a stabilizing effect on the pressure, thus eliminating the need for a special interpolation when the incompressible limit is reached. The reformulation of the equations in a characteristics co-moving frame provides a consistent artificial diffusion when the spatial discretization is done. This diffusion, similar to that of the SUPG methods, can handle the purely numerical oscillations which usually appear when the Galerkin method is applied to equations with dominant convective terms.

2. The algorithm

2.1. Navier–Stokes equations

The equations that model the behavior of a Newtonian fluid are the Navier–Stokes equations, derived from general conservation principles of mass, momentum and energy. A simplified version of these equations can be written as the continuity equation (e.g. Batchelor, 1967; Faber, 1995),

$$\frac{\partial \rho}{\partial t}+\frac{\partial U_i}{\partial x_i}=0, \tag{1}$$

the momentum equation,

$$\frac{\partial U_j}{\partial t}+\frac{\partial (u_i U_j)}{\partial x_i}+\frac{\partial}{\partial x_i}(\delta_{ij}p-\tau_{ij})+\rho g_j=0, \tag{2}$$

and the heat equation,

$$\frac{\partial T}{\partial t}+u_i\frac{\partial T}{\partial x_i}-\frac{1}{c_v\rho}\frac{\partial}{\partial x_i}\left(k\frac{\partial T}{\partial x_i}\right)-\frac{1}{c_v\rho}\sigma_{ij}\frac{\partial u_i}{\partial x_j}=0. \tag{3}$$

Table 1
List of symbols used in paper. We also employ $f^{n+\vartheta}\equiv\vartheta f^{n+1}+(1-\vartheta)f^n$ and $\Delta f^n\equiv f^{n+1}-f^n$ for any function f. Superscript denotes time-step level. Bold vectors stand for vectors of nodal unknowns, and $\vec{\mathbf{F}}_i$ denotes vector which is known at moment of solving particular equation

Latin symbols	
a	major axis (ellipsoidal chamber)
b	minor axis (ellipsoidal chamber)
c	speed of the sound
c_v	heat capacity per unit of mass
F_s	safety factor
$\vec{g}$	gravity vector
H	heat flux
H_0	computational conduit height
H_c	magma chamber depth
k	thermal conductivity
m	solubility law exponent
$\vec{n}$	unit normal vector
p	pressure
P_c	critical (exsolution) pressure
Q	gas constant
R	residual
r	conduit radius
s	solubility law constant
$\vec{t}$	traction vector
t	time
T	temperature
$\vec{u}$	velocity vector
$\vec{U}$	momentum vector
$\hat{U}$	fractional momentum vector
W	test function for the momentum
$\hat{W}$	test function for the fractional momentum
W_P	test function for the continuity equation
W_T	test function for the heat equation
wt%	volatile mass fraction
Greek symbols	
α	factor in Eq. (35)
ΔP	magma overpressure
Δt	time step size
Γ	contour of Ω
μ	viscosity
ρ	density
ρ_g	gas density
ρ_l	liquid density
σ_{ij}	Cauchy stress tensor components
τ_{ij}	deviatoric Cauchy stress tensor components
θ	heavyside function
ϑ_i	parameters of the algorithm
Ω	domain

In these equations (see Table 1 for notation) t is time, ρ is density, U_i and u_i are the ith component of the momentum and velocity vectors, respectively (i.e., $U_i = \rho u_i$), p is the pressure, g_i is the ith component of the gravity vector, σ_{ij} and τ_{ij} are the components of the Cauchy stress tensor and its deviatoric (i.e. $\tau_{ij} = \sigma_{ij} - p\delta_{ij}$), k is the thermal conductivity, T is the temperature and c_v is the heat capacity per unit of mass. In all the equations that appear in this paper, indices run from 1 to 2 or 3 (space dimensions) and repeated indices always imply summation. Assuming the Stokes hypothesis, the deviatoric stress tensor τ_{ij} is linearly related to velocity gradients by

$$\tau_{ij} = \mu\left(\frac{\partial u_i}{\partial x_j} + \frac{\partial u_j}{\partial x_i} - \frac{2}{3}\frac{\partial u_k}{\partial x_k}\delta_{ij}\right) \tag{4}$$

where μ is the viscosity. Adding a state law

$$\varphi(\rho, T, p) = 0 \tag{5}$$

it is possible to solve Eqs. (1)–(5) numerically.

2.2. Time discretization

It can be shown that when a scalar equation like:

$$\frac{\partial V}{\partial t} = -u_i\frac{\partial V}{\partial x_i} - L(V) = R(V) \tag{6}$$

is time discretized along the characteristics using a traditional finite-differences scheme one gets

$$\frac{V^{n+1} - V^n}{\Delta t} = R(V)^{n+\vartheta} - \frac{\Delta t}{2}u_i^n\frac{\partial R(V)^n}{\partial x_i}, \tag{7}$$

where V is the unknown function, the superscripts denote the time step level, Δt is the time step size, $\vartheta \in [0, 1]$ is a parameter, $f^{n+\vartheta} \equiv \vartheta f^{n+1} + (1-\vartheta)f^n$ for any function f and $R(V)$ is the residual. We will later show how the term that is proportional to Δt in Eq. (7) becomes a SUPG-like term when the space discretization is done, i.e. is a term that produces a stabilizing effect in those equations with convective terms by adding numerical diffusion along the streamlines in a consistent manner. We use Eq. (7) to discretize in time both the momentum equation, Eq. (2), and the heat equation, Eq. (3), because these equations contain convective terms that could lead to numerical instabilities. This leads to the time discretized continuity equation:

$$\frac{\Delta\rho^n}{\Delta t} = -\frac{\partial U_i^{n+\vartheta_1}}{\partial x_i}, \tag{8}$$

the time discretized momentum equation:

$$\frac{\Delta U_i^n}{\Delta t} = M_i^{n+\vartheta_3} - \frac{\partial p^{n+\vartheta_2}}{\partial x_i} - \frac{\Delta t}{2}u_k^n\frac{\partial R_i^n}{\partial x_k}, \tag{9}$$

where M_i and the ith component of the residual R_i are defined as:

$$M_i \equiv -\frac{\partial}{\partial x_j}(\rho u_i u_j - \tau_{ij}) - \rho g_i, \tag{10}$$

$$R_i \equiv M_i - \frac{\partial p}{\partial x_i}, \tag{11}$$

and the time discretized heat equation:

$$\frac{\Delta T^n}{\Delta t} = R_T^{n+\vartheta_4} - \frac{\Delta t}{2}u_k^n\frac{\partial R_T^n}{\partial x_k}, \tag{12}$$

where the residual of the heat equation R_T is defined as:

$$R_T \equiv -u_i\frac{\partial T}{\partial x_i} + \frac{1}{c_v\rho}\frac{\partial}{\partial x_i}\left(k\frac{\partial T}{\partial x_i}\right) + \frac{1}{c_v\rho}\sigma_{ij}\frac{\partial u_i}{\partial x_j}. \tag{13}$$

In these equations $\Delta f^n \equiv f^{n+1} - f^n$ for any function f and ϑ_1, ϑ_2, ϑ_3 and $\vartheta_4 \in [0, 1]$ are parameters introduced during the discretization. We will later show how, depending on its values, the algorithm becomes explicit, semi-implicit or implicit.

2.3. Splitting of the momentum equation

The most significant feature of the numerical scheme proposed here is the splitting of the momentum equation, Eq. (9), a technique first suggested by Chorin (1967, 1969) for incompressible flows. If the concept of splitting is applied to compressible flows one could have a single algorithm able to deal equally well with both regimes and using the same interpolation spaces for all of the unknowns. Let us introduce the ith component of the fractional momentum $\hat{U}_i$ as:

$$\hat{U}_i^{n+1} \equiv U_i^{n+1} + \Delta t\frac{\partial p^{n+\vartheta_2}}{\partial x_i}. \tag{14}$$

Using Eq. (14), Eqs. (8) and (9) can be rewritten as:

$$\frac{\Delta\hat{U}_i^n}{\Delta t} = M_i^{n+\vartheta_3} - \frac{\Delta t}{2}u_k^n\frac{\partial R_i^n}{\partial x_k}, \tag{15}$$

$$\frac{\Delta\rho^n}{\Delta t} = -\frac{\partial}{\partial x_i}\left(U_i^n + \vartheta_1\Delta\hat{U}_i^n - \vartheta_1\Delta t\frac{\partial p^{n+\vartheta_2}}{\partial x_i}\right), \tag{16}$$

$$\frac{\Delta U_i^n}{\Delta t} = \frac{\Delta\hat{U}_i^n}{\Delta t} - \frac{\partial p^{n+\vartheta_2}}{\partial x_i}. \tag{17}$$

We first compute the fractional momentum using Eq. (15), then the density (or the pressure) using Eq. (16) and finally the momentum by using Eq. (17). A deeper insight into the implicit treatment of M_i in Eq. (15) can be achieved by separating its convective and viscous parts, defined, respectively, as:

$$M_{c,i} \equiv -\frac{\partial}{\partial x_i}(\rho u_i u_j) = -\frac{\partial}{\partial x_j}(u_j U_i) \tag{18}$$

$$M_{\mathrm{v},i} \equiv \frac{\partial}{\partial x_j}\tau_{ij} \tag{19}$$

so that $M_i = M_{\mathrm{c},i} + M_{\mathrm{v},i} - \rho g_i$. In order to avoid the need to solve a nonlinear problem within each time step we take

$$M_{\mathrm{c},i}^{n+\vartheta_3} = -\frac{\partial}{\partial x_j}\left(u_j^n U_i^{n+\vartheta_3}\right), \tag{20}$$

so that the convective velocity is evaluated at the previous time step. This is a popular approach adopted in order to linearize the convective term for incompressible flows (e.g. Simo and Armero, 1994). In principle, the term $M_i^{n+\vartheta_3}$ in Eq. (15) should be computed using U_i^{n+1}. If this is done, Eqs. (15)–(17) are exactly equivalent to Eqs. (8) and (9). However, the use of U_i^{n+1} in Eq. (15) prevents the possibility of directly computing the fractional momentum from this equation, because at this moment U_i^{n+1} is still an unknown that will be computed later, in Eq. (17). This can be avoided by replacing $M_i^{n+\vartheta_3}$ by $\hat{M}_i^{n+\vartheta_3}$, which is obtained by computing M_i with $\hat{U}_i^{n+1}$ instead of U_i^{n+1}. Obviously, this introduces an splitting error. Nevertheless, using Eqs. (14) and (20) it is found that, up to second-order accuracy for the pressure term

$$M_{\mathrm{c},i}^{n+\vartheta_3} = \hat{M}_{\mathrm{c},i}^{n+\vartheta_3} + \vartheta_3\Delta t\frac{\partial}{\partial x_j}\left(u_j^n\frac{\partial p^n}{\partial x_i}\right). \tag{21}$$

The last term in Eq. (21) corrects the splitting error in the convective fluxes and only that corresponding to the viscous fluxes remains. In summary: we first compute the fractional momentum using Eq. (15) and replacing $M_i^{n+\vartheta_3}$ by $\hat{M}_i^{n+\vartheta_3}$. This can be done directly by computing M_i with $\hat{U}_i^{n+1}$ instead of V_i^{n+1} or using Eq. (21). The second option gives more accuracy because it reduces the inherent splitting error.

2.4. Weak form and boundary conditions

The next step is to obtain the weak form of Eqs. (12) and (15)–(17) by projecting these time-discretized equations into the usual space of test functions and integrating then over the domain Ω. Integrals with spatial second-order derivates are integrated by parts.

2.4.1. Fractional momentum equation

Multiplying Eq. (15) by the ith component of the test function for the fractional momentum $\hat{W}_i$, integrating over Ω, integrating by parts the viscous term and the term coming from the discretization along the characteristics and assuming that $R_i^n = 0$ on Γ, we get:

$$\begin{aligned}
&\int_\Omega \hat{W}_i\frac{\Delta\hat{U}_i^n}{\Delta t}\,\mathrm{d}\Omega \\
&= \int_\Omega \hat{W}_i\hat{M}_{\mathrm{c},i}^{n+\vartheta_3}\,\mathrm{d}\Omega - \vartheta_3\Delta t\int_\Omega \frac{\partial\hat{W}_i}{\partial x_j}u_j^n\frac{\partial p^n}{\partial x_i}\,\mathrm{d}\Omega \\
&\quad + \vartheta_3\Delta t\int_\Gamma n_j u_j^n\hat{W}_i\frac{\partial p^n}{\partial x_i}\,\mathrm{d}\Gamma - \int_\Omega\frac{\partial\hat{W}_i}{\partial x_j}\tau_{ij}^{n+\vartheta_3}\,\mathrm{d}\Omega \\
&\quad + \int_\Gamma \hat{W}_i n_j\hat{\tau}_{i,j}^{n+\vartheta_3}\,\mathrm{d}\Gamma + \int_\Omega\hat{W}_i\rho g_i\,\mathrm{d}\Omega \\
&\quad + \frac{\Delta t}{2}\int_\Omega\frac{\partial}{\partial x_k}(u_k^n\hat{W}_i)R_i^n\,\mathrm{d}\Omega,
\end{aligned} \tag{22}$$

where n_j is the jth component of the unit outward normal to Γ. The last term in Eq. (22) comes from the discretization along the characteristics. If $\nabla\cdot u^n = 0$ this term introduces an artificial diffusion similar to the one introduced by the SUPG method. The only difference is that the intrinsic time of the SUPG method is here replaced by a linear function of time. In Eq. (22), the integration by parts has led us to a boundary integral of the deviatoric stress tensor τ_{ij} contracted with the normal at the contours. As reflected in Eq. (4), for Newtonian fluids, τ_{ij} is a linear combination of the first derivatives of velocity and, therefore, to impose any value on $n_j\hat{\tau}_{ij}$ in Eq. (22) can be considered as a Neumann boundary condition for the velocity (momentum). This boundary condition can also be weakly prescribed in terms of traction. Then, apart from the prescription of the velocity (momentum) itself, we can also consider the following possibilities:

1. The whole traction vector $\vec{t}$ prescribed on Γ_{T}, i.e. $t_i = -pn_i + n_j\tau_{ij}$ given in Γ_{T}. This allows us to replace the boundary integral

$$\int_\Gamma \hat{W}_i n_j\hat{\tau}_{ij}^{n+\vartheta_3}\,\mathrm{d}\Gamma \tag{23}$$

appearing in Eq. (22) with

$$\int_{\Gamma-\Gamma_{\mathrm{T}}}\hat{W}_i n_j\hat{\tau}_{ij}^{n+\vartheta_3}\,\mathrm{d}\Gamma + \int_{\Gamma_{\mathrm{T}}}\hat{W}_i(t_i + p^n n_j)\,\mathrm{d}\Gamma. \tag{24}$$

2. Only the pressure component of the traction prescribed on Γ_{P}, that is, $t_i^{\mathrm{P}} = -pn_i$ given in Γ_{P}.

2.4.2. Continuity equation

Let us now consider Eq. (16) and weight it by a test function W_{P}, giving:

$$\int_\Omega W_P \frac{\Delta\rho^n}{\Delta t}\,d\Omega = -\int_\Omega W_P \frac{\partial U_i^n}{\partial x_i}\,d\Omega + \vartheta_1 \int_\Omega \frac{\partial W_P}{\partial x_i}\left(\Delta\hat{U}_i^n - \Delta t \frac{\partial p^{n+\vartheta_2}}{\partial x_i}\right) d\Omega - \vartheta_1 \int_\Gamma W_P n_i \left(\Delta\hat{U}_i^n - \Delta t \frac{\partial p^{n+\vartheta_2}}{\partial x_i}\right) d\Gamma, \quad (25)$$

As a boundary condition for the continuity equation we impose that the normal component of Eq. (17) also be verified on the boundary Γ, a condition equivalent to impose that the normal component of the momentum equation, Eq. (9), be verified on the boundary Γ. This leads to:

$$n_i\left(\Delta\hat{U}_i^n - \Delta t \frac{\partial p^{n+\vartheta_2}}{\partial x_i}\right) = n_i \Delta U_i^n \quad (26)$$

on the part of the boundary Γ_C where the test function W_P for the continuity equation does not vanish. On the other hand, the normal component $n_i\Delta U_i^n$ is known on the part of the boundary Γ_D where the momentum is given, so that

$$\int_\Gamma W_P n_i\left(\Delta\hat{U}_i^n - \Delta t \frac{\partial p^{n+\vartheta_2}}{\partial x_i}\right) d\Gamma = \int_{\Gamma_C} W_P n_i\left(\Delta\hat{U}_i^n - \Delta t \frac{\partial p^{n+\vartheta_2}}{\partial x_i}\right) d\Gamma = \int_{\Gamma_D} W_P n_i \Delta U_i^n\,d\Gamma. \quad (27)$$

The boundary condition introduced by Eq. (27) can then be considered as the normal component of the momentum equations.

2.4.3. Momentum equation

For Eq. (17), after weighting by the ith component of the test function for the momentum W_i we obtain:

$$\int_\Omega W_i \frac{\Delta U_i^n}{\Delta t}\,d\Omega = \int_\Omega W_i \frac{\Delta\hat{U}_i^n}{\Delta t}\,d\Omega - \int_\Omega W_i \frac{\partial p^{n+\vartheta_2}}{\partial x_i}\,d\Omega. \quad (28)$$

2.4.4. Heat equation

Let us now weight Eq. (12) using a test function W_T, integrate the diffusion term by parts, set $R_T = 0$ on Γ and prescribe the conduction heat flux to H on a part of the boundary Γ_H. For simplicity, we assume an explicit time approximation along the characteristics, i.e. we assume $\vartheta_4 = 0$ in Eq. (12). The result is:

$$\int_\Omega W_T \frac{\Delta T^n}{\Delta t}\,d\Omega = \int_\Omega W_T\left[\left(-u_i + \frac{k}{c_v\rho^2}\frac{\partial\rho}{\partial x_i}\right)\frac{\partial T}{\partial x_i}\right]^n d\Omega + \int_\Omega W_T\left(\frac{1}{c_v\rho}\sigma_{ij}\frac{\partial u_i}{\partial x_j}\right)^n d\Omega - \int_\Omega \frac{\partial W_T}{\partial x_i}\left(\frac{k}{c_v\rho}\frac{\partial T}{\partial x_i}\right)^n d\Omega + \frac{\Delta t}{2}\int_\Omega \frac{\partial}{\partial x_k}(u_k^n W_T) R_T^n\,d\Omega + \int_{\Gamma_H} \frac{1}{c_v\rho^n} W_T H\,d\Gamma. \quad (29)$$

In Eq. (29), Dirichlet conditions are imposed directly on $\Gamma - \Gamma_H$ and Newman conditions (the heat flux H) are imposed by computing the boundary integral

$$\int_{\Gamma_H} \frac{1}{c_v\rho^n} W_T H\,d\Gamma. \quad (30)$$

2.5. Discrete problem

Once the weak form of the differential equations is established, we can proceed to discretize the space. We use the standard Galerkin FEM in which all the test functions $\hat{W}_i$, W_P, W_i and W_T in Eqs. (22), (25), (28) and (29) are taken to be equal to the shape functions. Once the spatial discretization has been performed the equations can be written in matrix form:

$$\mathbf{M}\frac{\Delta\vec{\hat{\mathbf{U}}}^n}{\Delta t} = \vec{\mathbf{F}}_1 - \mathbf{K}\vec{\hat{\mathbf{U}}}^{n+\vartheta_3} \quad (31)$$

$$\mathbf{M}_\alpha\frac{\Delta\vec{\mathbf{P}}^n}{\Delta t} + \vartheta_1\Delta t\mathbf{L}\vec{\mathbf{P}}^{n+\vartheta_2} + \vec{\mathbf{F}}_2, \quad (32)$$

$$\mathbf{M}\frac{\Delta\vec{\mathbf{U}}^n}{\Delta t} = \mathbf{M}\frac{\Delta\vec{\hat{\mathbf{U}}}^n}{\Delta t} - \mathbf{G}\vec{\mathbf{P}}^{n+\vartheta_2} + \vec{\mathbf{F}}_3, \quad (33)$$

$$\mathbf{M}_S\frac{\Delta\vec{\mathbf{T}}^n}{\Delta t} = \vec{\mathbf{F}}_4, \quad (34)$$

where $\vec{\hat{\mathbf{U}}}$, $\vec{\mathbf{P}}$, $\vec{\mathbf{U}}$ and $\vec{\mathbf{T}}$ are the vectors of nodal unknowns and $\mathbf{M}$, $\mathbf{M}_S$, $\mathbf{K}$ and $\mathbf{G}$ are, respectively, the standard mass matrix for vectorial unknowns, the standard mass matrix for scalar unknowns, the matrix arising from the viscous and convective terms in the fractional momentum equation and the matrix coming from the gradient operator. Here and later we will use $\vec{\mathbf{F}}$ to denote a vector which is known at the moment of

solving a particular equation. The matrices $\mathbf{M}_\alpha$ and $\mathbf{L}$ in Eq. (32) are defined as:

$$\mathbf{M}_{\alpha,ij} \equiv \int_\Omega \alpha N_i N_j \, d\Omega \tag{35}$$

$$\mathbf{L}_{ij} \equiv \int_\Omega \frac{\partial N_i}{\partial x_k}\frac{\partial N_j}{\partial x_k} \, d\Omega \tag{36}$$

where N_i is the shape function associated with the ith node of the finite element mesh and α depends on the state law.

2.6. State law

In this section we discuss the dependence of the values of α adopted in Eq. (35) on the kind of flow. Although we will apply the algorithm to model the withdrawal of magma from a shallow chamber, let us first consider other flows frequently encountered in engineering and geological applications such as incompressible flow,

$$\rho \text{ constant} \tag{37.1}$$

slightly compressible flow,

$$\frac{\partial \rho}{\partial t} = \frac{1}{c^2}\frac{\partial p}{\partial t}, \tag{37.2}$$

and perfect gas,

$$p = \rho Q T, \tag{37.3}$$

where c is the speed of the sound and Q is a gas constant. Using pressure as the variable and substituting Eqs. (37.1), (37.2) and (37.3) in the LHS of Eq. (25) one obtains the following values for α in the discrete equation, Eq. (32):

$$\begin{aligned} &\alpha = 0 \quad \text{for incompressible flows,} \\ &\alpha = \frac{1}{c^2} \quad \text{for slightly compressible flows,} \\ &\alpha = \frac{1}{QT^{n+1}} \quad \text{for perfect gases.} \end{aligned} \tag{38}$$

For high viscosity magmas above the exsolution level and below the fragmentation level, the mixture can be considered as a bubbly flow, characterized by a liquid continuum with dispersed gas bubbles and crystals in thermal and mechanical equilibrium (Papale, 1996). In this bubbly flow regime the gas bubbles and the liquid can be considered to move with the same velocity along the conduit (Sparks, 1978). A suitable state law for the mixture in the bubbly flow regime domain inside the magma chamber and in the lowermost part of the conduit, is (Folch et al., 1998):

$$\rho = \frac{\rho_l}{1 + ((\rho_l Q T)/P)((\text{wt\%} - sP^m)/(1 - sP^m))\theta(P_c - P)}, \tag{39}$$

where ρ is the mixture density, ρ_l is the liquid density (here assumed to be a constant), T is the temperature, wt% is the volatile mass fraction (water for felsic magmas), s and m are solubility constants and θ is the step function (defined as $\theta = 0$ for $P \geq P_c$ and $\theta = 1$ for $P \leq P_c$). The critical pressure P_c at which gas exsolution begins depends only on the volatile mass fraction (e.g. Tait et al., 1989):

$$P_c = \left(\frac{\text{wt\%}}{s}\right)^{1/m}. \tag{40}$$

Below this critical pressure, where the magma is not vesiculated, we have $\theta = 0$ in Eq. (39) and the density is that of the liquid. Fig. 1 shows the mixture density predicted by Eq. (39) for a rhyolitic magma with $\rho_l = 2400$ kg/m^3 at $T = 850$°C. Following Tait et al. (1989), values of $s = 4.11 \times 10^{-6}$ Pa$^{-1/2}$ and $m = 0.5$ for H_2O in a rhyolitic melt are assumed. Note how the mixture density is constant below the exsolution level and decreases progressively above this level due to volatile exsolution induced by the pressure decrease. Note also that Eq. (39) is dependent on temperature. Nevertheless, magmas have a large thermal capacity whereas the host rock has a low thermal conductivity, so that temperature variations inside the chamber occur over a timescale orders of magnitude greater than the duration of an eruption (Dobran, 1992). In consequence, one may assume T to be a constant and one can assume that Eq. (39) conforms to a barotropic state law. The value of α for Eq. (39) may then be obtained approximately by multiplying Eq. (39) by p^{n+1}/p^n, so that:

$$\alpha = \frac{\rho_l}{p^n + \rho_l Q T((\text{wt\%} - s(p^n)^m)/(1 - s(p^n)^m))\theta(p_c - p^n)}. \tag{41}$$

2.7. General features and discussion

We have introduced four different parameters $\vartheta_i \in [0, 1]$ that depending on their values yield fully implicit, semi-implicit or fully explicit solutions to the algorithm (see Table 2). We consider for simplicity $\vartheta_4 = 0$ for the heat equation. The parameter ϑ_1 appears in the time-discretized continuity equation and controls both the temporal precision, which is maximum when $\vartheta_1 = 1/2$, and the additional stabilizing artificial diffusion, which is maximum when $\vartheta_1 = 1$ and vanishes when $\vartheta_1 = 0$. The parameter ϑ_2 is introduced during the splitting of the momentum equation. When zero, the algorithm is fully explicit when ϑ_3 is also zero, or semi-implicit if ϑ_3

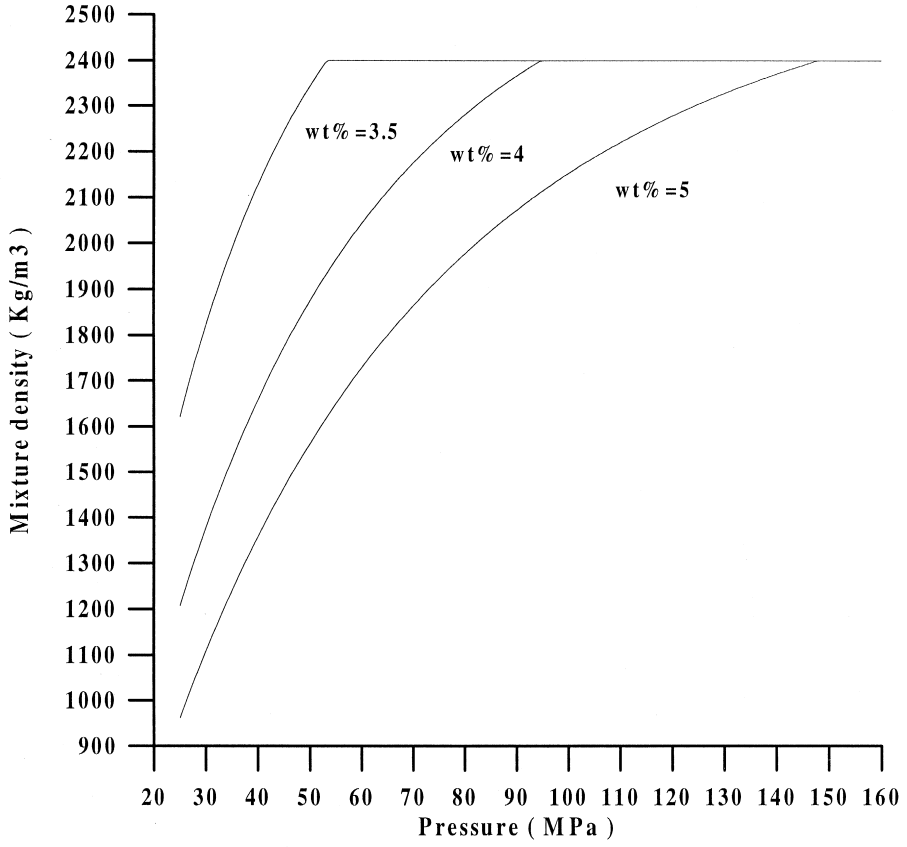

Fig. 1. Mixture density versus pressure given by state law equation, Eq. (39). Results for rhyolitic magma with $T = 850°C$, $\rho_l = 2400$ kg/m^3 and water contents of 3.5, 4.0 and 5.0 wt%, respectively. Note how position of exsolution level, where mixture density becomes constant equal to ρ_l, depends on water content.

is not zero. If ϑ_2 is not zero, the continuity equation is solved implicitly but the algorithm can also be semi-implicit if $\vartheta_3 \neq 0$. Finally, the parameter ϑ_3 appears during the discretization of the momentum equation. It controls whether the viscous and convective terms of this equation are treated explicitly (if $\vartheta_3 = 0$) or implicitly (if $\vartheta_3 \neq 0$). To summarise, if $\vartheta_2 = \vartheta_3 = 0$ the algorithm is fully explicit and if $\vartheta_2 = 0$ and $\vartheta_3 \neq 0$ it is semi-implicit. Neither the explicit nor the semi-implicit forms of the algorithm deal with the incompressible

Table 2
Characteristics of algorithm depending on values of ϑ_2 and ϑ_3. We have assumed $\vartheta_4 = 0$ for energy equation (explicit treatment). Parameter ϑ_1 can have any value in [0, 1]

ϑ_2	ϑ_3	Algorithm	Variables
0	0	fully explicit	only ρ can be used as unknown; not possible for incompressible flows
Continuity equation, Eq. (32), is explicit	$0 < \vartheta_3 \leq 1$	*semi-implicit*, Eq. (31) is implicit	
$0 < \vartheta_2 \leq 1$	0	*semi-implicit*, Eq. (31) is explicit	either p or ρ can be used for compressible flows, but only p for incompressible
Continuity equation, Eq. (32), is implicit	$0 < \vartheta_3 \leq 1$	*fully implicit*	

situation because the pressure must be treated implicitly for incompressible flows. If $0 < \vartheta_2 \leq 1$ the scheme is either semi-implicit (if $\vartheta_3 = 0$) or fully implicit (if $\vartheta_3 \neq 0$) and either pressure or density can be considered as unknowns, except at the incompressible limit. Each time step is calculated as follows:

1. Calculate a time increment Δt.
2. Solve the heat equation, Eq. (34), to obtain $\vec{\mathbf{T}}^{n+1}$ (if necessary).
3. Calculate the fractional momentum $\hat{\vec{\mathbf{U}}}^{n+1}$ using Eq. (31).
4. Solve the continuity Eq. (32) for $\vec{\mathbf{P}}^{n+1}$.
5. Calculate the density $\vec{\boldsymbol{\rho}}^{n+1}$ using the state law.
6. Calculate the momentum $\vec{\mathbf{U}}^{n+1}$ using Eq. (33).

We use the critical time step given by the 1D convection–diffusion equation (Hirsch, 1990):

$$\Delta t = \frac{F_s}{(4\varepsilon/h^2) + (|\vec{u}|/h)}, \tag{42}$$

where F_s is a safety factor (less than 1 in the explicit scheme) and h is the characteristic element dimension. For the continuity equation $\varepsilon = 0$, whereas for the momentum equation $\varepsilon = \mu/\rho$. We compute the time step at each node of the FEM mesh for each equation and use the minimum value throughout the mesh.

3. A numerical example

The algorithm developed here can be applied to a broad range of problems in engineering and geological fluid dynamics. Numerical examples under different flow regimes such as incompressible, slightly compressible, barotropic or perfect gas can be found, for example, in Zienkiewicz et al. (1995), Zienkiewicz and Codina (1995), Vázquez et al. (1996) and Codina et al. (1998). In this paper we use the algorithm to model the withdrawal of magma from a shallow chamber.

Let us consider a central vent eruption with axial symmetry as shown in Fig. 2. The entire domain comprises a magma chamber at depth H_c and a central conduit of radius r along the symmetry axis. Assuming axial symmetry and using cylindrical coordinates, we solve the three-dimensional problem like a two-dimensional one. The problem is considered as thermally uncoupled. Water is assumed to be the only volatile phase, because it is by far the most abundant gas species in felsic magmas. Water content is set as a par-

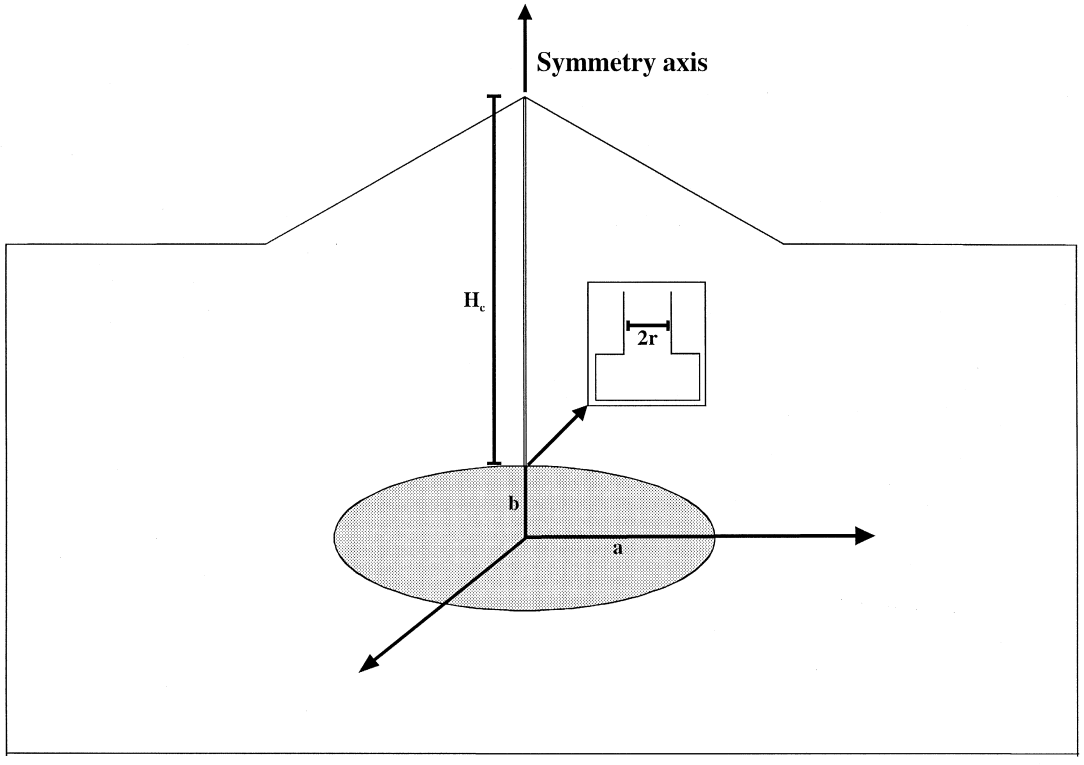

Fig. 2. Central vent eruption with axial symmetry. Elliptical magma chamber with major axis a and minor axis b is located at depth H_c below Earth's surface. Magma flows through conduit of radius r that coincides with symmetry axis.

ameter of the model and its exact value is imposed once the magma chamber depth and the lithostatic pressure have been assumed. We choose a water content sufficient to ensure that the chamber contents are partially vesiculated prior to eruption, in order to reproduce the situation of an eruption triggered by crystallisation-driven volatile oversaturation. The computational outlet is set a few hundred meters above the lower conduit entrance and therefore does not coincide with the physical outlet, the vent. The pressure at the computational outlet is set at lithostatic, despite the fact that conduit models predict a drop in magma pressure below lithostatic inside the conduit (Papale and Dobran, 1993, 1994). We stop the computational domain inside the conduit in order to ensure the validity of Eq. (39), i.e. in order to keep the flow within the bubbly regime. Boundary and initial conditions are illustrated schematically in Fig. 3. The non-slip condition is imposed at the chamber walls and the horizontal component of the velocity is set to zero at the symmetry axis. The magma is considered to be at rest before the eruption. The initial pressure distribution is assumed to be lithostatic, with an overpressure inside the chamber equal to the tensile strength of the host rock. The eruption rate is obtained by computing the integral

$$\int_S \rho \vec{v}\, \mathrm{d}\vec{s} \tag{43}$$

over the conduit section S, where ρ is given by Eq. (39) and $\vec{v}$ is the velocity. The area below the eruption-rate curve plotted versus time gives the total mass erupted. The position of the exsolution level is given by the critical pressure P_c. Substituting typical magma values into Eq. (42), we get $\Delta t \approx F_s/10$, so that the maximum time-step able to ensure the stability of the algorithm is small. Due to this limitation we performed all of the simulations using the fully implicit option ($\vartheta_2 = \vartheta_3 = 1$), where F_s could achieve values up to 20 without any problem of stability. Note that Eq. (32) cannot be solved explicitly (with $\vartheta_2 = 0$) because the flow is incompressible in some parts of the domain.

The results shown in this section are obtained by applying the model to a particular situation. It should

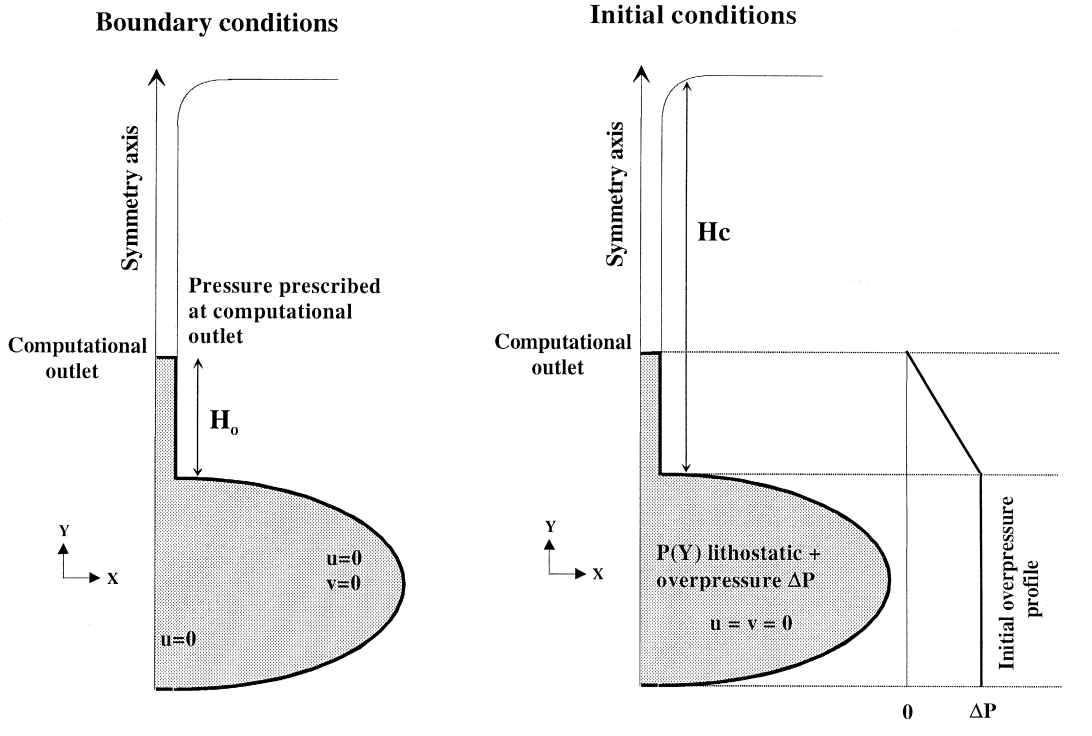

Fig. 3. Schematic cartoon showing boundary and initial conditions. Computational domain in grey. Pressure is prescribed to lithostatic at computational outlet, which is located at depth H_0 above conduit entrance. No-slip condition ($u = v = 0$) imposed at chamber walls. Initial pressure profile is lithostatic plus overpressure ΔP. This overpressure is driving force for triggering eruption and is assumed to be equal to tensile strength of the host rock and to decrease linearly along conduit.

be said that, from a physical point of view, this model presents some limitations because it assumes a magma with constant viscosity as well as a chemically homogeneous magma composition. Despite these limitations, the model is useful not only to test the algorithm but also to obtain a preliminary approach to this complex physical process. A rhyolitic magma with $\rho_l = 2400$ kg/m^3, $T = 850°C$ and $\mu = 10^5$ is assumed. The magma chamber is an ellipsoid with a major axis $a = 2.5$ km, a minor axis $b = 0.5$ km, a volume $V = 4/3\pi a^2 b \cong 14$ km^3 and a conduit radius of 25 m. We utilized a mesh comprising 3080 linear elements (3190 nodes). The initial pressure in the chamber is equal to lithostatic, plus an overpressure $\Delta P = 10$ MPa. This overpressure is typical of the tensile strength of volcanic rocks (Touloukian et al., 1981). The lithostatic pressure at the computational outlet is set to 105 MPa. The results show that the overpressure decreases exponentially as the eruption proceeds, until it becomes zero and the eruption stops. This is a general behaviour found in any other simulation (Folch et al., 1998). This pressure decrease produces a drop in the exsolution level, so that deeper parts of the chamber become progressively volatile-oversaturated. Thus, the upper, oversaturated magma layer becomes progressively thicker and less dense. Fig. 4 shows the eruption rate for this particular simulation using water contents of 4.5 and 5.0 in wt%. In all of the numerical experiments, the eruption rate reaches a peak immediately after the onset of the eruption and then decreases exponentially as the eruption proceeds. In this particular example, a total erupted mass of approximately 3×10^{12} kg is obtained. This value is comparable with those found for explosive volcanic eruptions: 0.6×10^{12} kg for the 1980 Mount St. Helens eruption (Scandone and Malone, 1985), 5–73×10^{12} kg for the Nisyros eruption (Barberi et al., 1988) and 8.6×10^{12} kg for the 79 A.D. Vesuvius eruption (Barberi et al., 1981). Fig. 5 shows the position of the exsolution level versus time for water contents of 4.3 and 4.5 wt%. For wt% = 4.3 the exsolution level, which is initially located 275 m below the conduit entrance, drops approximately 300 m in 22 h. Fig. 6 shows the velocity field at the conduit entrance after 22 h of eruption. A commonplace feature found during

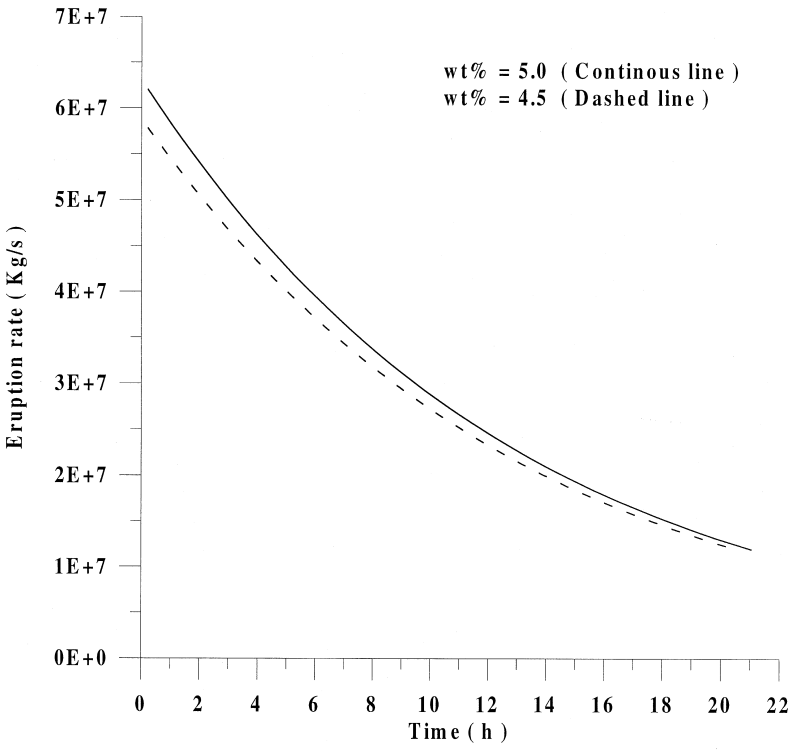

Fig. 4. Eruption rate versus time. Results for initial overpressure $\Delta P = 10$ MPa, viscosity $\mu = 10^5$ Pa s, liquid density $\rho_l = 2400$ kg/m^3 and water contents of 4.5 and 5.0 wt%. Exponential decrease in mass discharge rate is only slightly dependent on volatile content.

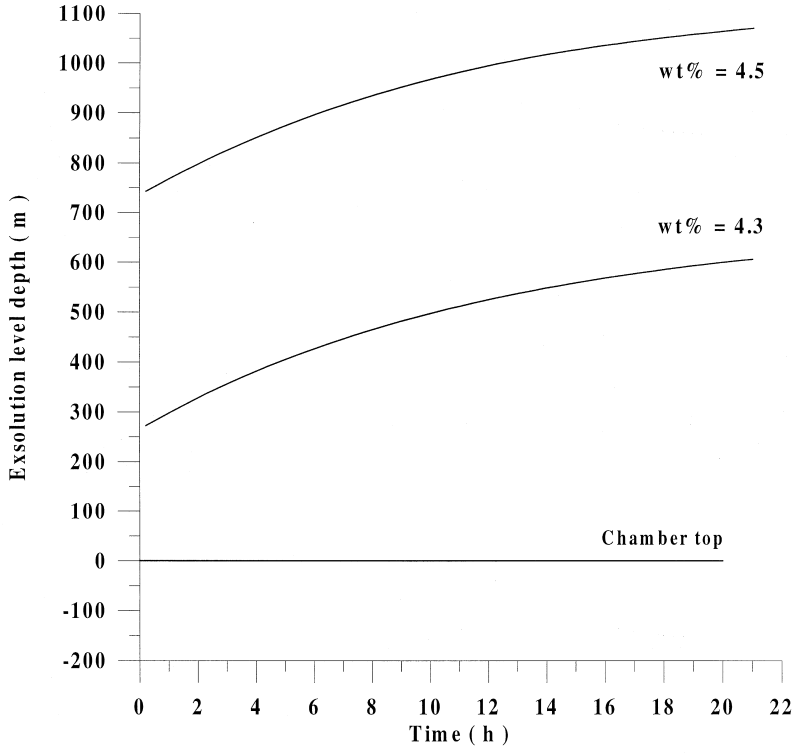

Fig. 5. Position of exsolution level. Origin of vertical axis set at top of chamber. Same parameters as in Fig. 4, but with water contents of 4.3 and 4.5 wt%. Note that shape of functions does not differ substantially when water content is changed. However, increasing volatile contents produces movement of exsolution level.

the withdrawal of magma from chemically homogeneous chambers is that the magma reaches the conduit entrance laterally. Note that although the velocity field is unsteady, its changes are given in a characteristic time of hours, so that at any instant we can approach the streamlines by the trajectories. A volume of magma reaching the conduit entrance is partly erupted through the conduit and partly reinjected back into the chamber. Thus, a volume of magma initially emplaced at the top of the chamber moves first laterally to the vicinity of the conduit entrance and is then either erupted or forced to descend hundreds of meters back into the chamber before again moving up. As this magma descends, the exsolved volatiles within it are progressively re-dissolved back into the magma as the pressure raises increases their solubility in the melt. This phenomenon has an important consequence: as we have assumed that the magma behaves as an incompressible flow below the exsolution level, any inflow into the undersaturated incompressible layer must produce an equal outflow to ensure the conservation of mass. This movement is transmitted through viscous stresses, so that eventually, the entire magma chamber is affected by this induced movement.

4. Summary and discussion

We have developed an algorithm that numerically solves the Navier–Stokes equations using a finite-element method. The algorithm uses a fractional-step method which allows the use of equal interpolation spaces for the pressure and velocity fields and produces a stabilizing effect on the pressure, eliminating the need for a special interpolation at the incompressible limit. This algorithm can be used to model many problems in geological fluid dynamics. We apply it to characterize the withdrawal of shallow magma chambers during explosive volcanic eruptions. The results show that the pressure at the conduit entrance decreases exponentially as the eruption proceeds. This decrease in pressure produces a drop in the exsolution level, so that deeper parts of the chamber become progressively volatile-oversaturated with time. The total

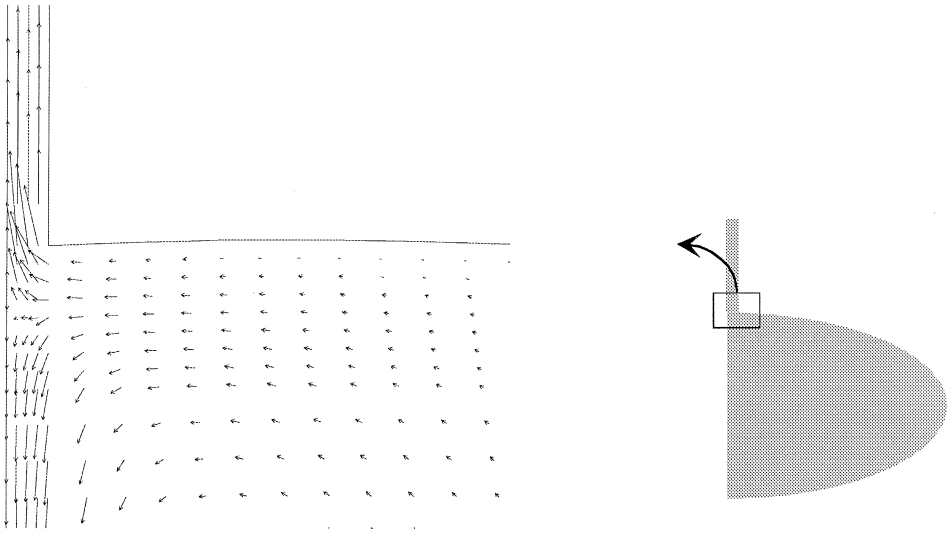

Fig. 6. Velocity field at conduit entrance after 22 h of simulated eruption using the same chamber geometry and magma properties as for Figs. 4 and 5. Although velocity field is unsteady, its temporal variations are slow and one can approach streamlines by trajectories. Note how a volume of magma reaches conduit entrance laterally and is then either erupted or reinjected back into the chamber.

mass erupted is in good agreement with the results of Bower and Woods (1997), who found that for volatile-saturated magma chambers a mass fraction of 0.01–0.1 of the initial mass will be erupted. In general, we deduce that for chambers with similar volume and magma properties, the qualitative behavior does not change substantially when different chamber geometries are considered. However, the quantitative behavior does vary slightly. The total erupted mass increases as the chamber becomes flatter, because flattened chambers have a large volumetric fraction of compressible oversaturated magma. A small change in the initial volatile content does not change the mass discharge rate substantially, but has an important influence on the position of the exsolution level. A small increase in volatile content produces a substantial drop in the exsolution level, which reaches deeper parts of the chamber. The total erupted mass does not depend on the viscosity, although the viscosity plays a major role in controlling the duration and the peak intensity of the eruption. An increase in the initial overpressure, associated in the model with the tensile strength of the host rock, produces an increase in the total downward displacement of the exsolution level. In consequence, when the initial overpressure is high, a greater mass is erupted because a greater volumetric fraction of magma changes from volatile-undersaturated and incompressible to volatile-oversaturated and compressible during the withdrawal process.

Acknowledgements

This research has been founded by the EC contract ENV-CT96-0259 and the CICYT Project AMB96-0498-C04. A.F. is grateful for a CIRIT research fellowship. We also thank Professor Yuen, an anonymous reviewer and Giray Ablay for their comments on this paper.

References

Barberi, F., Bizourard, H., Clocchiatti, R., Metrich, N., Santacroce, R., Sbrana, A., 1981. The Somma-Vesuvius magma chamber: a petrological and volcanological approach. Bulletin of Volcanology 44, 295–315.

Barberi, F., Navarro, J., Rosi, M., Santacroce, R., Sbrana, A., 1988. Explosive interactions of magma with ground water: insights from xenoliths and geothermal drillings. Rendo. Soc. Itl. Mineral. Petrol. 43, 901–926.

Batchelor, G., 1967. An Introduction to Fluid Dynamics, 1st ed. Cambridge University Press, Cambridge, 615 pp.

Blake, S., 1981. Volcanism and dynamics of open magma chambers. Nature 289, 83–785.

Blake, S., 1984. Volatile oversaturation during the evolution of silicic magma chambers as an eruption trigger. Journal of Geophysical Research 89 (B10), 8237–8244.

Bower, S., Woods, A., 1997. Control of magma volatile content and chamber depth on the mass erupted during explo-

sive volcanic eruptions. Journal of Geophysical Research 102 (B5), 10273–10290.

Chorin, A.J., 1967. A numerical method for solving incompressible viscous problems. Journal Computational Physics 2, 12–26.

Chorin, A. J., 1969. On the convergence of discrete approximation to the Navier–Stokes equations. Mathematical Computation 23, 745–762.

Codina, R., Vázquez, M., Zienkiewicz, O., 1998. A general algorithm for compressible and incompressible flow. Part III. The semi-implicit form. International Journal for Numerical Methods in Fluids 27, 13–32.

Dobran, F., 1992. Nonequilibrium flow in volcanic conduits and application to the eruptions of Mt. St. Helens on May 18, 1980, and Vesuvius in AD 79. Journal of Volcanology and Geothermal Research 49, 85–311.

Faber, T., 1995. Fluid Dynamics for Physicists. Cambridge University Press, Cambridge, 440 pp.

Folch, A., Martí, J., Codina, R., Vázquez, M., 1998. A numerical model for temporal variations during explosive central vent eruptions. Journal of Geophysical Research 103 (B9), 20883–20899.

Hirsch, C., 1990. Numerical Computation of Internal and External Flows. John Wiley & Sons, New York, 740 pp.

Papale, P., 1996. Modeling of magma ascent along volcanic conduits: a review. Environment and Climate Programme. European Commission, Brussels, pp. 3–40.

Papale, P., Dobran, F., 1993. Modeling of the ascent of magma during the plinian eruption of Vesuvius in AD 79. Journal of Volcanology and Geothermal Research 58, 101–132.

Papale, P., Dobran, F., 1994. Magma flow along the volcanic conduit during the Plinian and pyroclastic flow phases of the May 18, 1980, Mount St. Helens eruption. Journal of Geophysical Research 99, 4355–4373.

Scandone, R., Malone, S., 1985. Magma supply, magma discharge and readjustment of the feeding system of the Mount St. Helens during 1980. Journal of Volcanology and Geothermal Research 23, 239–262.

Simo, J., Armero, F., 1994. Unconditional stability and long behavior of transient algorithms for the incompressible Navier–Stokes equations. Computational Methods in Applied Mechanics and Engineering 111, 111–154.

Smith, R.L., 1979. Ash flow magmatism. American Geological Society 180, 5–27.

Sparks, R.S.J., 1978. The dynamics of bubble formation and growth in magmas: a review and analysis. Journal of Volcanology and Geothermal Research 3, 1–37.

Spera, F., 1984. Some numerical experiments on the withdrawal of magma from crustal reservoirs. Journal of Geophysical Research 89 (B10), 8222–8238.

Spera, F., Yuen, D., Greer, J., Sewell, G., 1986. Dynamics of magma withdrawal from stratified magma chambers. Geology 14, 723–726.

Tait, S., Jaupart, C., Vergniolle, S., 1989. Pressure, gas content and eruption periodicity of a shallow, crystallizing magma chamber. Earth and Planetary Science Letters 92, 107–123.

Touloukian, S., Judd, R., Roy, R., 1981. Physical Properties of Rocks and Minerals. McGraw-Hill, New York, 548 pp.

Trial, F., Spera, F., Greer, J., Yuen, D., 1992. Simulations of magma withdrawal from compositionally zoned bodies. Journal of Geophysical Research 97 (B5), 6713–6733.

Vázquez, M., Codina, R., Zienkiewicz, O., 1996. A fractional step method for the solution of the Navier–Stokes equations. Internal Report. CIMNE, Barcelona, 103 pp.

Zienkiewicz, O., Codina, R., 1995. A general algorithm for compressible and incompressible flow. Part I. The split, characteristic-based scheme. International Journal for Numerical Methods in Fluids 20, 869–885.

Zienkiewicz, O., Morgan, K., Satya, B., Codina, R., Vázquez, M., 1995. A general algorithm for compressible and incompressible flow. Part II. Tests on the explicit form. International Journal for Numerical Methods in Fluids 20, 887–913.